Nanoscale

Accepted Manuscript

This article can be cited before page numbers have been issued, to do this please use: M. Ries, F. Nippert, B. März, M. Alonso-Orts, T. Grieb, R. Hötzel, P. Hille, P. Emtenani, E. Akinoglu, E. Speiser, J. Plaickner, J. Schörmann, M. Auf der Maur, K. Müller-Caspary, A. Rosenauer, N. Esser, M. Eickhoff and M. R. Wagner, *Nanoscale*, 2023, DOI: 10.1039/D2NR05529E.

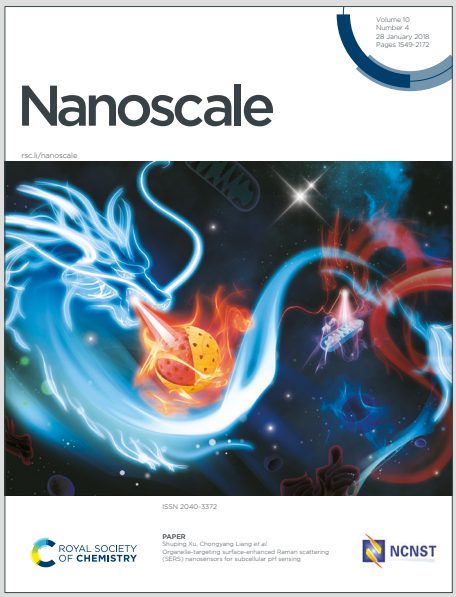

ROYAL SOCIETY OF CHEMISTRY

rsc.li/nanoscale

View Article Online
DOI: 10.1039/D2NR05529E

View Article Online
DOI: 10.1039/D2NR05529E

Journal Name

ARTICLE TYPE

Cite this: DOI: 00.0000/xxxxxxxxxx

Origin of spectral red-shift and polarization patterns of self-assembled InGaN nanostructures on GaN nanowires

Maximilian Ries,[ab] Felix Nippert,[a] Benjamin März,[cd] Manuel Alonso-Orts,[e] Tim Grieb,[ef] Rudolfo Hötzel,[e] Pascal Hille,[e] Pouria Emtenani,[a] Eser Metin Akinoglu,[b] Eugen Speiser,[b] Julian Plaickner,[bg] Jörg Schörmann,[h] Matthias Auf der Maur,[i] Knut Müller-Caspary,[d] Andreas Rosenauer,[ef] Norbert Esser,[ab] Martin Eickhoff,[e] and Markus R. Wagner*[aj]

Received Date
Accepted Date

DOI: 00.0000/xxxxxxxxxx

The luminescence of $In_xGa_{1-x}N$ nanowires (NWs) is frequently reported with large red-shifts as compared to the theoretical value expected from the average In-content. Both, compositional fluctuations and radial built-in fields were considered accountable for this effect, depending on the size, structure, composition, and surrounding medium of the NWs. In the present work, the emission properties of InGaN/GaN NWs grown by plasma-assisted molecular beam epitaxy are investigated in a comprehensive study combining ultraviolet-Raman and photoluminescence spectroscopy (PL) on vertical arrays, polarization-dependent PL on bundles of few NWs, scanning transmission electron microscopy, energy-dispersive X-ray spectroscopy, and calculations of the band profiles. The roles of inhomogeneous In-distribution and radial fields in the context of optical emission properties are addressed. The radial built-in fields are found to be modest, with a maximum surface band-bending below 350 meV. On the other hand, variations in the local In-content have been observed that give rise to potential fluctuations whose impact on the emission properties is shown to prevail over band-bending effects. Two luminescent bands with large positive and moderate negative polarization ratio of approximately $\approx +80\%$ and $\leq -60\%$, respectively, were observed. The red-shift in luminescence is associated with In-rich inclusions in the NWs due to thermodynamic decomposition during growth. The negative polarization anisotropy is suggested to result from spontaneously formed superlattices in the In-rich regions of the NWs. The NWs show a preferred orthogonal absorption due to the dielectric boundary conditions and highlight the extreme sensitivity of these structures towards light polarization.

1 Introduction

Semiconductor nanowires (NWs) have become a vivid field of research in the last two decades. The large variety of different

[a] Technische Universität Berlin, Institut für Festkörperphysik, Hardenbergstraße 36, 10623 Berlin, Germany
[b] Leibniz-Institut für Analytische Wissenschaften – ISAS e.V., Department Interface Analytics, Schwarzschildstraße 8, 12489 Berlin, Germany
[c] Ernst-Ruska-Centre for Microscopy and Spectroscopy with Electrons at Forschungszentrum Jülich, Wilhelm-Johnen-Str., 52425 Jülich, Germany
[d] Department of Chemistry and Centre for NanoScience, Ludwig-Maximilians-Universität München, Butenandtstr. 11, 81377 Munich, Germany
[e] Universität Bremen, Institut für Festkörperphysik, Otto-Hahn-Allee 1, 28359 Bremen, Germany
[f] Universität Bremen, MAPEX Center for Materials and Processes, Bibliothekstr. 1, 28359 Bremen, Germany
[g] Helmholtz-Zentrum Berlin für Materialien und Energie GmbH, Hahn-Meitner-Platz 1, 14109 Berlin, Germany
[h] Justus-Liebig-Universität Gießen, I. Physikalisches Institut und Zentrum für Materialforschung (LaMa), Heinrich-Buff-Ring 16, 35392 Gießen, Germany
[i] University of Rome Tor Vergata, Department of Electronic Engineering, Via del Politecnico 1, 00133 Rome, Italy
[j] Paul-Drude-Institut für Festkörperelektronik, Leibniz-Institut im Forschungsverbund Berlin e.V., Hausvogteiplatz 5–7, 10117 Berlin, Germany

View Article Online
DOI: 10.1039/D2NR05529E

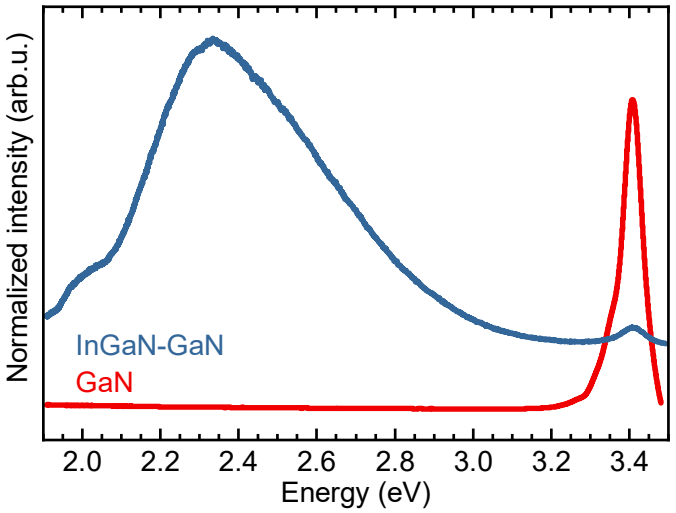

Fig. 1 Photoluminescence spectra of as-grown GaN and InGaN/GaN NW ensembles recorded at 300 K. The spectra are offset for clarity.

growth techniques in combination with their promising properties such as high crystalline quality,[1] one-dimensionality,[2] and variability for functionalization makes semiconductor NWs interesting for a wide field of applications ranging from transistors and solar energy harvesting,[3] light emitting diodes and laser diodes,[1,4–6] to photodetectors, waveguides,[4,7] and optochemical sensors.[8–10] III-V-NWs have raised particular interest due to the tunability of the direct bandgap and improved material quality compared to bulk material.[1,11] It has been shown that InGaN NW light emitting diodes exhibit a reduced Auger recombination rate, i.e., lower efficiency droop,[3] compared to bulk InGaN or InGaN quantum wells (QW).

Both, owing to the crystal symmetry and peculiarities of the geometry, luminescence emitted from semiconductor NWs exhibits a distinct polarization dependence which can be of importance for the application in single photon emitters as well as in imaging and display technologies.[4,12] The depolarization ratio ρ compares the intensities of parallel ($I_{\parallel}$) and orthogonally ($I_{\perp}$) polarized emission with respect to the NW axis:

$$\rho = \frac{I_{\parallel} - I_{\perp}}{I_{\parallel} + I_{\perp}} \,. \tag{1}$$

In the case of III-nitrides, polarization anisotropy has been found in both photoluminescence (PL) and electroluminescence measurements of pure GaN NWs and those with embedded InGaN nanodiscs (NDs).[5,13–16] Interestingly, these anisotropies contradict the expected ratio from dipole selection rules of excitonic transitions.

Two main mechanisms have been identified to be of relevance for the polarization anisotropy in quasi one-dimensional sample geometries: (i) quantum-mechanical confinement and (ii) dielectric confinement.[2] The latter leads to a preponderating emission of light with polarization along the nanowire axis and a positive ρ. The contribution of these effects is mainly based on the diameter of the respective NW and the dielectric contrast between the NW and the surrounding medium. As a rule of thumb, once the actual diameter of the NW exceeds the exciton Bohr radius, the first effect drastically weakens. For InGaN, the exciton Bohr radius is commonly expected to be around $3-10$ nm, depending on the In-content.[17] For NWs of larger diameter, the second, purely classical effect dominates, until the NW diameter becomes large enough to be comparable to bulk material.[2] Depolarization ratios of GaN NWs with embedded InGaN QWs[5,18–23] and quantum dots (QD) are frequently reported,[12,24–26] but not for InGaN NWs. Especially in structures containing QDs-in-a-wire, i.e., embedded regions that act as QDs, the emission properties can differ strongly due to non- or semi-polar side-facets and the emission typically shows polarization perpendicular to the NW axis.[24,25]

This study reports the composition, influence of radial electric fields, and polarization anisotropy of luminescence light emitted from $In_xGa_{1-x}N$ NWs grown on top of GaN NWs in a self-assembled process. The PL energy differs significantly from what is expected for the average In-concentration as determined by X-ray diffraction (XRD) analysis. The origin of this red-shift is discussed with respect to compositional fluctuations and band-bending effects. The depolarization ratio reaches values as high as $+90\%$ at approximately 2 eV. An additional higher energy luminescence band is observed that exhibits a negative ρ. The origin of this band is addressed, and experimentally observed higher intensities for excitation with polarization perpendicular to the NW axis are discussed.

2 Results and discussion

This work reports measurements on two different kinds of samples: (i) as-grown, vertically-aligned arrays of NWs and (ii) bundles of few NWs isolated from the as-grown samples. Scanning electron microscopy analysis of as-grown GaN NWs yields lengths of 1400 nm in total. In the base region they exhibit a diameter of 30 nm and growth proceeds along the $[000\bar{1}]$-direction. With increasing lengths, the coalescence between neighboring wires increases. For the as-grown GaN NW array, the average diameter of coalesced wires at the top is 80 ± 10 nm. The GaN base part in InGaN/GaN NW arrays has a length of ≈ 1100 nm. The InGaN part is grown on top with a length of approximately 370 nm. The growth details for the base part are identical to those of GaN NWs and can be found in the experimental section. For the InGaN part, the diameter gradually increases to 110 ± 10 nm towards the top.

The following part is divided into four sections: (i) PL and Raman measurements of as-grown vertically-aligned NW arrays, (ii) PL experiments on bundles of few NWs, (iii) scanning transmission electron microscopy (STEM) and energy-dispersive X-ray spectroscopy (EDX) analysis, and (iv) calculations of the band-bending.

2.1 (i) Photoluminescence and Raman spectra of vertically-aligned arrays

In Figure 1, the room temperature PL spectra of as-grown InGaN/GaN NW arrays (blue) are compared to the luminescence of GaN NWs (red). The GaN spectrum is characterized by the bandgap luminescence at 3.4 eV. The spectra of InGaN/GaN NWs exhibit a broad emission band between $2.0-2.8$ eV. Such a broad PL emission band in the visible range indicates an inhomogeneous

View Article Online
DOI: 10.1039/D2NR05529E

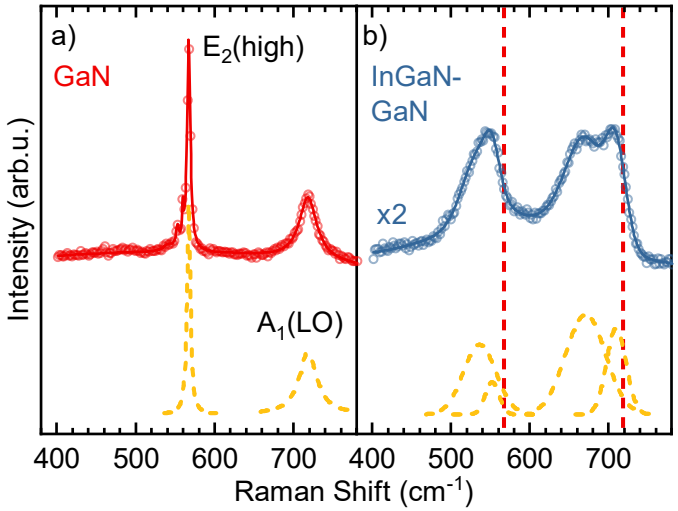

Fig. 2 UV-Raman spectra recorded from a) as-grown GaN (red) and b) as-grown InGaN/GaN NWs (blue) at 300 K. The yellow dashed lines indicate the individual fit components and solid lines the corresponding fits. Red vertical broken lines correspond to the position of the GaN NW E_2(high) and A_1(LO), respectively. The InGaN/GaN NW spectrum has been corrected by a Gaussian contribution to the background.

In-distribution in the NWs and differences from one NW to the other. The peak position of the dominating band corresponds to an In-content of $25-30\%$.[27]

On the same two samples, ultraviolet (UV)-Raman spectroscopy was performed. The first-order modes observed for as-grown GaN NWs in Figure 2a) are the E_2(high) at 567 cm^{-1} and the longitudinal optical (LO) phonon A_1(LO) at 718 cm^{-1}, see also Table 1. The E_2(high)-frequencies are close to the literature value of strain-free GaN (568 cm^{-1}).[28] However, the A_1(LO) shifts significantly from the expected position at 734 cm^{-1}.[28] The shift of the NW Raman modes to lower wavenumbers compared to bulk data is a result of phonon confinement,[29–31] and of excitation above the fundamental bandgap energy.[32] The NW sidewalls form boundaries that confine the phonons and lead to uncertainty in the associated wavevector. The larger shift of the A_1(LO) originates from the steeper slope in the phonon dispersion, whereas the E_2(high) dispersion is rather flat.[33]

UV-Raman spectra of the as-grown InGaN/GaN NWs in Figure 2b) are characterized by an E_2(high) peak at 552 cm^{-1} with low-frequency shoulders at 536 and an A_1(LO) structure consisting of two peaks at 710 cm^{-1} and 671 cm^{-1}, respectively. Concerning the as-grown InGaN/GaN NWs, the excitation wavelength has strong implications on the scattering volume: photons with energy below the InGaN bandgap penetrate deep into the NW material, probing both the InGaN and GaN part, while photons with 266 nm are mainly absorbed in the InGaN part.

Table 1 Raman active modes from as-grown GaN and InGaN/GaN NWs for 266 nm (UV) excitation, see Figure 2, and references.

Sample	E_2(high) cm^{-1}	A_1(LO) cm^{-1}
GaN	567	718
InGaN/GaN	536 552	671 710
Refs.[28,33]	568	734

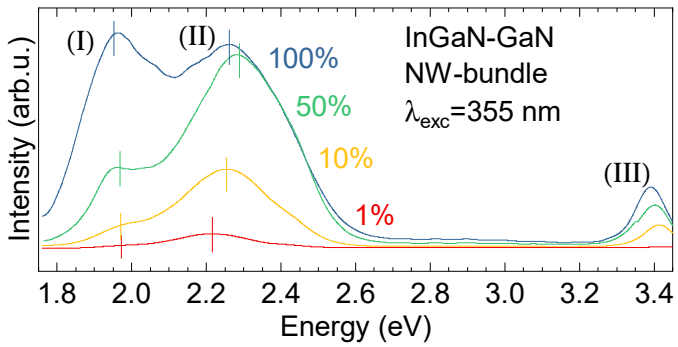

Fig. 3 Photoluminescence spectra recorded from an isolated InGaN/GaN bundle dispersed on a glass substrate at 300 K, excited with different power densities at 355 nm. 100% corresponds to a laser power of ≈ 1.7 mW on the sample. The luminescence bands are labeled by Roman numbers and the respective peak positions are marked by vertical bars.

The frequency shift of the ternary $In_xGa_{1-x}N$ NWs E_2(high) at 552 cm^{-1} yields an In-distribution centered at around $x \approx 22\%$.[34] Considering the enlarged diameter of the $In_xGa_{1-x}N$ wire segment, the frequency shift due to phonon confinement can be neglected, so the A_1(LO) phonon frequency of 710 cm^{-1} translates directly to a value of $x \approx 16\%$.[34] The differing values obtained from the E_2(high) and A_1(LO) phonon modes highlight the inhomogeneity of the material and the complexity to relate a Raman shift to an In-content.

The low-frequency peak of the A_1(LO) structure at 671 cm^{-1} suggests the occurrence of $In_xGa_{1-x}N$ with higher In-content x, which is also indicated by a low-frequency shoulder of the E_2(high) at 532 cm^{-1}. Both peak positions yield $x \approx 40\%$.[34] Surface optical modes, providing another possible explanation for the low-frequency A_1(LO) peak, should be located significantly above the observed mode at 671 cm^{-1}, which is not the case.[35–37]

2.2 (ii) PL of isolated nanowire bundles

Figure 3 presents excitation power-dependent PL-spectra of a bundle with more than ten InGaN/GaN NWs dispersed on a glass substrate. Each PL spectrum consists of a GaN part, peak (III), at around 3.4 eV, and an InGaN part between 1.8 eV and 2.6 eV. The latter band is composed of two contributions centered at around 2.0 and 2.3 eV, labeled (I) and (II), respectively. Each color represents a different excitation power, starting with 100% or at around 1.7 mW (blue) down to 1% (red). The GaN PL red-shifts with increasing excitation power density and resulting laser-heating. A similar behavior is observed for the lower energy feature (I). The main peak (II) follows the opposite trend. Its transition energy increases, and the peak area saturates, most likely due to screening of the internal piezo-electric field by the photogenerated charge carriers. This implies that the screening overcompensates the temperature-dependent red-shift. This behavior is not expected from homogenous wires, but indicates the occurrence of compositional fluctuations.[38]

In the following, the polarization anisotropy of two different

View Article Online
DOI: 10.1039/D2NR05529E

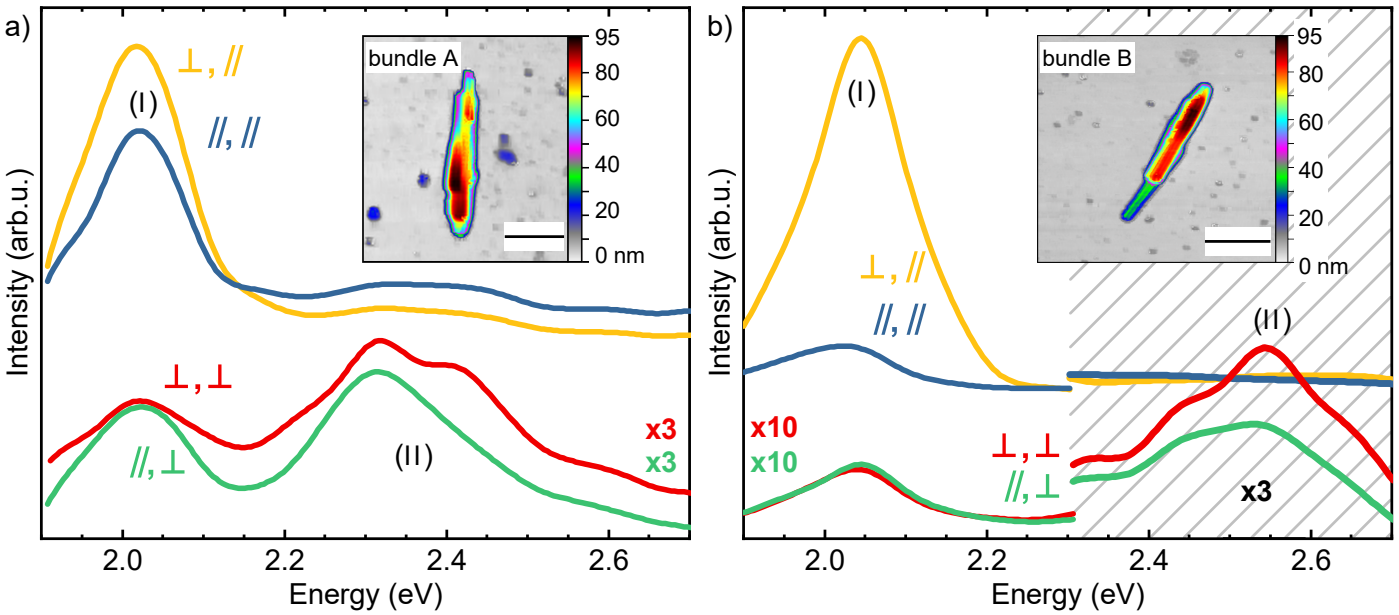

Fig. 4 Polarized PL spectra from two InGaN/GaN NW bundles (bundle A in a), bundle B in b)) on silicon in the $1.9-2.7$ eV range for 355 nm laser excitation at room temperature. The spectra are offset for clarity, and a Savitzky-Golay filter was applied. The Polarization (X,Y) was controlled for both incoming (X) and outgoing light (Y) either parallel ($\parallel$) or orthogonal ($\perp$) to the wire. The laser power was set to ≈ 1 mW. The insets show AFM height profiles of the respective bundle. The scale bars represent 500 nm, respectively. Note that the y-axis for orthogonal collection is magnified by a factor of 3 in a) and 10 in b), while the gray hatched part in b) is magnified by an additional factor of 3.

bundles with less than 10 NWs will be compared. The respective PL spectra are shown in Figure 4 together with atomic force microscopy (AFM) images. The excitation power was approximately 1 mW and corresponds to 75% in Figure 3. The depolarization ratio is mainly determined by the emission properties. Although the polarization anisotropy is stronger in perpendicular absorption and less prominent in the parallel case, as summarized in Table 2, the sign of the ratio is determined by the emission rather than the absorption. The difference in the depolarization ratio for perpendicular or parallel excitation, i.e., absorption, can be ascribed to the dielectric boundary conditions and is extremely sensitive to diameter, refractive indices, and wavelength.[2]

E	$\boldsymbol{E}_{exc}$	bundle A		bundle B	
eV		ρ	$\overline{\rho}$	ρ	$\overline{\rho}$
(I)	$\parallel$	37	51 ± 11	64	80 ± 5
2.0 eV	$\perp$	65		96	
(II)	$\parallel$	-36	-56 ± 10	-33	-34 ± 13
$2.2-2.6$ eV	$\perp$	-75		-35	

Table 2 Depolarization ratios ρ and mean value $\overline{\rho}$ for the two bands observed in the polarized PL spectra (Figure 4) for both excitation polarizations $\boldsymbol{E}_{exc}$. The uncertainty of each peak area is estimated as 15% from comparing the GaN peak area between several measurements.

The InGaN-related part of both bundles exhibits two peaks. They have a dominating emission at around 2.0 eV, band (I), with a high mean depolarization ratio $\overline{\rho}$ of up to 80% and a second emission band (II) at around $2.2-2.6$ eV with a moderate negative $\overline{\rho}$ below -60%, the latter being hardly noticeable in bundle B. The mean depolarization ratio is the average value from the two excitation polarizations. It is important to note that the excitation energy of 3.4 eV determines the absorption anisotropy, while the respective PL energy yields the emission anisotropy, i.e., $2.0-2.6$ eV. The structure of the two bundles is different. From the AFM insets, one can see that bundle B consists of at least two wires that are coalesced around the center. The bundle A in Figure 4a) has the same height, but the structure is less clear. The elevated part presumably at the bottom segment indicates additional NWs in this bundle.

In most reported cases on polar NWs, the luminescence is strongly polarized parallel to the NW axis, i.e., $\rho >> 0$.[5,12,22] In this case, this is true for band (I), but the depolarization ratio of the higher energy band (II) is negative. Chen et al. ascribed the reduced depolarization ratio for thicker, i.e., coalesced GaN NWs to defect-related emission from localized excitons, rather than free exciton emission.[15] This reflects well the geometry of the NWs studied in this publication. However, it only explains a reduced $\overline{\rho}$ from one wire to another, but not the change in sign.

A possible origin is the existence of QD-like formations in the NWs, e.g., confined In-rich regions. It is well known from the literature, that so-called QDs-in-a-wire structures can exhibit large negative polarization anisotropy.[12,24,25] This possible assignment is supported by the Raman measurements indicating localized regions with high In-content that most likely give rise to the low-frequency peak of the A_1(LO) structure, c.f. Fig. 2.

2.3 (iii) STEM and EDX analyses

STEM analyses show that not all NWs are identical. They differ in length, diameter, and degree of coalescence. From comparative measurements we conclude that the In-content is also not

View Article Online
DOI: 10.1039/D2NR05529E

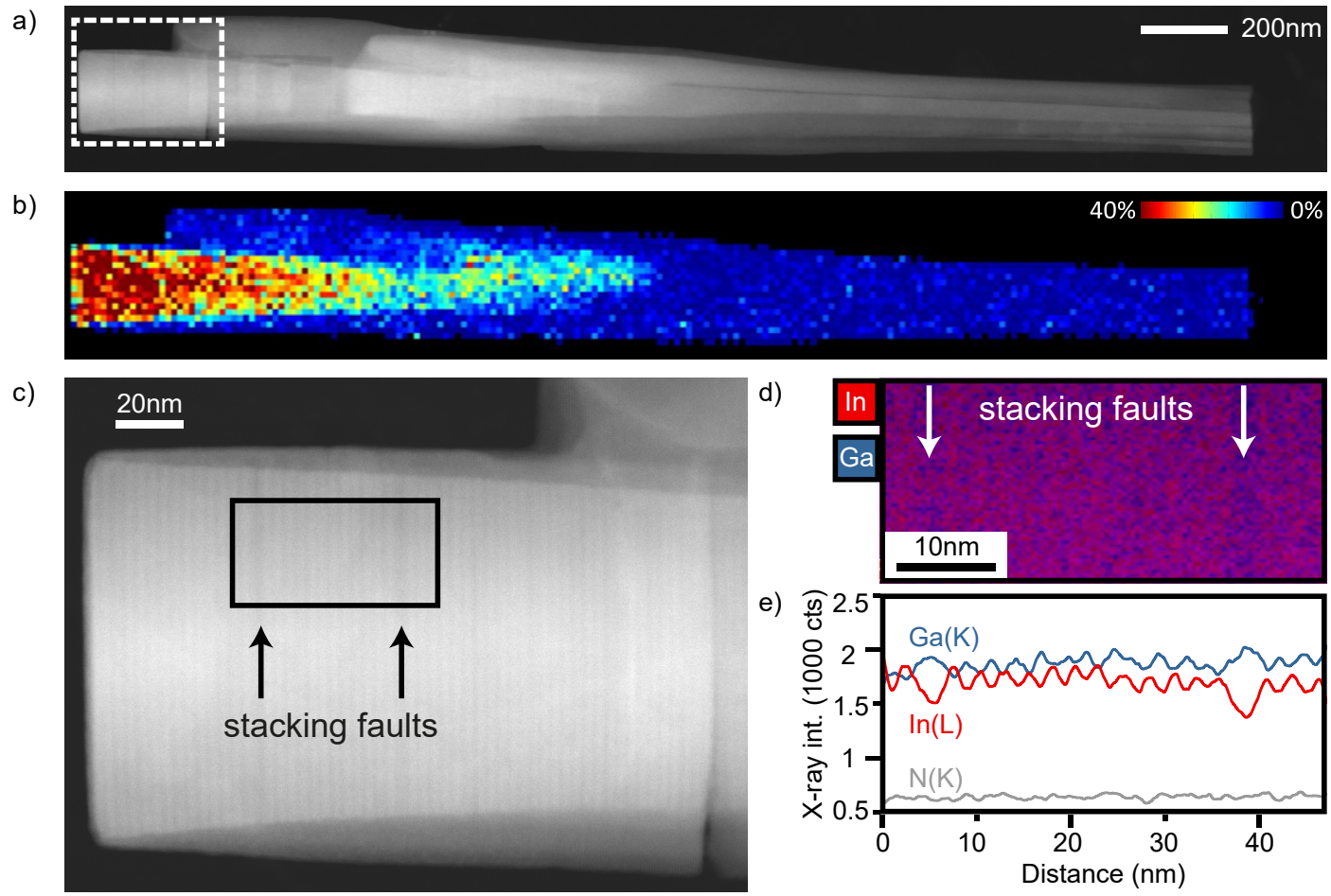

Fig. 5 a) ADF-STEM image of InGaN/GaN NWs. b) In-concentration from EDX (with In + Ga = 100%). c) Detail of the top part (white box) of the NW in a). The two characteristic stacking faults are marked by black arrows. d) Integrated high-resolution EDX peak intensities from the region in the black rectangle in c). Color-coded: In L lines - red; Ga K lines - blue. e) Ga(K), In(L), and N(K)-profiles from averaging the map in d).

the same in every NW.[39] However, there are characteristics that occur in the vast majority of NWs, which are well represented by the example shown in the annular-dark field STEM (ADF-STEM) image in Figure 5. The diameter increases from about 30 nm at the GaN base to $80-100$ nm at the InGaN part for a typical NW. The NWs in Figure 5a) show inclusions of brighter intensity that can be attributed to a region with higher In-concentration. This InGaN inclusion is surrounded by a shell, as it can be seen by the slightly darker ADF intensity around the inclusion. Further STEM analysis revealed no change in the crystal structure for this region compared to the rest of the NWs. In the shell, no significant amount of indium was found by EDX. Towards the apex, the In-concentration in the NWs increases to $30-40\%$.

Figure 5b) implies that the measured In-concentration decreases with increasing distance from the apex. These observations are supported by the results from Raman measurements, revealing a high In-content and a low In-content phase, respectively. However, the concentration gradient seen by EDX is largely due to the fact that the width of the GaN shell increases towards the base of the NWs, which leads to an effective reduction of the In-content measured with EDX.

Figure 5c) shows an ADF-STEM image of the upper part of the NWs in Figure 5a). It reveals an inner structure of the In-containing inclusion consisting of brighter and darker layers with a periodicity of about 2.2 nm. High contrast in the ADF-STEM images suggests a higher In-content based on two mechanisms. (i) The contrast strongly depends on the material's atomic number (Z-contrast) and (ii) static disorder affects electron scattering significantly. An EDX intensity map from the region inside the black rectangle in Figure 5c) is shown in Figure 5d) with the intensities of the In-L and Ga-K lines color-coded. From the profile in Figure 5e) it is visible that bright layers in the ADF image contain more indium compared to the darker layers. Due to a broadening of the STEM beam in the rather thick specimen and dynamical scattering effects, assigning an absolute composition to the EDX signal is a challenge that lies beyond the scope of the current study. However, it can be concluded that the In-content fluctuates across the layers periodically, complementary to the Ga-content. The two characteristic features marked by arrows in Figure 5c) and Figure 5d) are stacking faults. The STEM analysis proves the presence of a superlattice that is not related to defects, but defects were observed especially in the upper half of the wires. In general, the NWs comprise of the GaN base and the InGaN part, starting at the InGaN/GaN interface. This part is surrounded by a

View Article Online
DOI: 10.1039/D2NR05529E

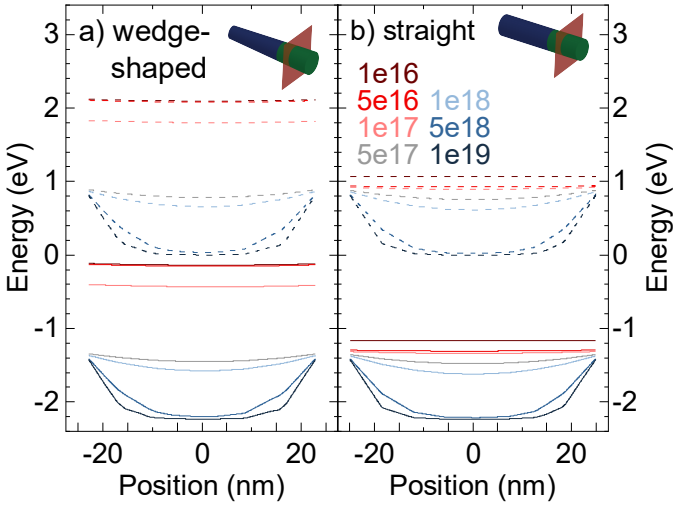

Fig. 6 Calculations of the valence (solid lines) and conduction band energies (broken lines) for different doping concentrations of $1\times10^{16}-1\times10^{19}$ cm^{-3} in a) tapered (left) and b) straight (right) $In_{0.3}Ga_{0.7}N$/GaN NWs. The density of the surface states was assumed to be 6×10^{14} cm^{-2} at energies consistent with Segev et al.[40] The NWs are assumed to be in air without surrounding electric fields. The insets show where the band profiles are extracted: 800 nm from the GaN base (blue), in the middle of the InGaN part (green). The intersection is visualized by a red plane.

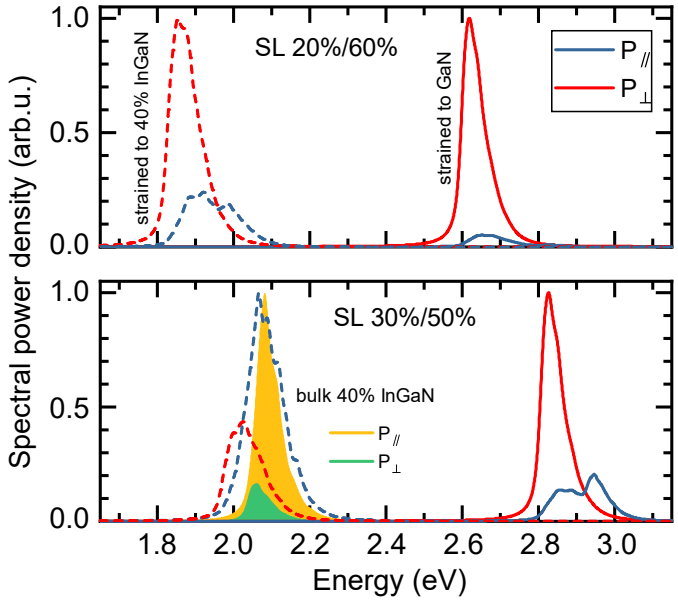

Fig. 7 1D-simulations of the spectral power density parallel and orthogonal to the NW c-axis in the electric-field approximation of a 20%/60%-InGaN superlattice (top) and a 30%/50%-InGaN superlattice (bottom) strained to 40%-InGaN and GaN, respectively. In the bottom panel, the yellow/green shaded areas correspond to bulk 40%-InGaN.

very thin GaN shell. The superlattice can be situated in between two InGaN parts or directly starting at the interface. In some cases, the top part is missing, however, this can be as well due to the dispersion of the nanowires via ultrasonication.

2.4 (iv) Calculations

To elucidate whether In-rich inclusions or surface-band-bending effects lead to the large luminescence red-shift, we performed band energy calculations with different doping levels.

Figure 6 depicts the calculated profiles of the lowest conduction and the topmost valence band edges along the diameter in single, freestanding InGaN/GaN NWs with a nominal In-concentration of 30%. Inclined sidewalls with increasing diameter towards the top in combination with the growth direction $(000\bar{1})$ lead to a discontinuity of the normal component of the polarization field across the side surface, inducing an equivalent negative surface charge. Bulk doping with a density above 1×10^{17} cm^{-3}, compensates for the polarization-induced surface charge, which becomes apparent from the realignment of the Fermi energy in Figure 6a).

The strain at the GaN-InGaN interface relaxes after <50 nm in both directions, thus piezoelectric effects exist only close to the interface. Consequently, the radial field close to the interface is slightly stronger compared to the center of the InGaN part. For low and moderate doping levels, the radial field is very small. Based on typical values for $n_e\approx0.1-1.0\times10^{18}$ cm^{-3},[39,41,42] the radial electric field induces a band-bending of less than 200 meV (for $In_{0.1}Ga_{0.9}N$/GaN NWs less than 350 meV), i.e., it can not explain the observed red-shift of the luminescence, which enforces the suggested existence of In-rich regions.

1D 8-band k·p simulation results for superlattices with alternating layers of 40%/60%-InGaN and 30%/50%-InGaN in Figure 7 underline the effect of strain on the emission characteristics of such structures. Both emission energy and dominant polarization depend crucially on the strain state of the nanowire, due to the strain induced band shifts. Fully strained to a surrounding GaN matrix, the orthogonal polarization dominates over the parallel case and the photoluminescence is strongly blue-shifted compared to the relaxed case (here 40%-InGaN). Furthermore, the emission characteristics approach the bulk case (yellow and green shaded areas) when the relaxation increases.

3 Conclusions

We have presented a comprehensive study of the structural and optical properties of InGaN nanostructures grown on GaN nanowires. By comparing the polarized PL spectra to the STEM-images in Fig. 5, we have demonstrated that the emission band (I) originates predominantly from the top part of the NW, while emission band (II) is caused by the superlattice emission surrounded by a GaN matrix from the part closer to the InGaN/GaN interface. The superlattices are not related to defects, but seem to originate from thermodynamic decomposition and inhomogeneous In-incorporation during growth. Summarizing the obtained results by PL, Raman, and STEM-EDX measurements, as well as band-energy calculations, we have presented evidence that surface-band-bending and a concomitant radial Stark effect play an inferior role in the observed red-shift of the luminescence of $In_xGa_{1-x}N$ NWs, instead, the dominating reason is the inhomogeneous In-incorporation during growth that can spontaneously form superlattices. Furthermore, we have demonstrated a pronounced polarization anisotropy of the emission most likely being related to the formation of the superlattice structures.

View Article Online
DOI: 10.1039/D2NR05529E

4 Experimental

InGaN/GaN NWs were grown in high-density vertical arrays by plasma-assisted molecular beam epitaxy on n-type Si(111) substrates using a self-assembled-growth process in nitrogen-rich conditions.[43,44] The NWs exhibit a hexagonal cross-section, corresponding to the wurtzite crystal structure with growth direction along the $(000\bar{1})$ direction.[45] The NW-density in the vertical arrays is in the order of $5-10\times10^9$ cm^{-2}. According to the PL data of single NWs previously reported,[39] and in comparison to reports from other groups the charge carrier density in the InGaN/GaN NWs can be assumed to be around $n_e \approx 0.1-1.0\times10^{18}$ cm^{-3}.[39,41,42] The substrate temperature during GaN growth was 770°C and 520°C during InGaN growth. Growth times were set to 90 min for the GaN base and 60 min for the InGaN part. Pure GaN NW arrays were grown similarly without the InGaN part. Single wires/small bundles were released by ultrasonication of as-grown NWs in iso-propanol for 60 s. The dispersed NWs were drop-casted onto specific substrates (natively oxidized Si(111) and glass) and identified by AFM measurements using a Park XE-100. Prior to PL measurements, the bundles were located with laser scanning and matched with the positions extracted from AFM. After successful PL measurements, the nanowire bundles were again imaged by AFM to guarantee that no structural changes occurred during optical measurements.

ADF-STEM imaging and EDX map data acquisition was conducted at 200 kV using a Hitachi HF5000 field emission STEM equipped with a dual Ultim® Max silicon drift detector system by Oxford Instruments. An area of 50.1 nm × 26.1 nm was scanned at a step size of 57 pm. The data set was 8×8 binned before peak deconvolution and display. The line scan was reconstructed from the original map data with applied 4×4 binning and a smoothing factor of 5.

Raman and PL spectra in the UV (266 nm, Nd:YAG) were recorded in back-scattering configuration using a Horiba T64000 spectrometer in single grating mode with a thermoelectrically cooled Synapse charge-coupled device. A UV-optimized 2400 lines/mm holographic grating with a spectral resolution of 4(2) cm^{-1} at 266 nm served as dispersing element. UV-Raman spectra were collected with an LMU-40X-UVB, NA=0.5 objective from Thorlabs. The spectra were calibrated to the Raman bands of β-Ga_2O_3 and atmospheric N_2 and O_2.

PL measurements with 355 nm were recorded with a 1800 lines/mm grating. The spectral resolution was around 0.5 meV at 3.492 eV. A Zeiss LD EC Epiplan-Neofluar x100 (NA=0.75) objective served to focus the light on the sample with a spot-size below 500 nm confirmed by confocal lateral laser scanning over a NW. The polarization of the excitation was controlled with a $\lambda/2$-plate behind the laser. The polarization dependence of the beamsplitter was taken into account. The emission polarization was rotated by a Fresnel rhomb to match the preferred configuration of the grating. A Rochon prism served as an analyzer in front of the spectrometer. The choice of these polarizing elements ensured stable polarization conditions over the entire spectral range. Measurements were performed with polarization parallel or perpendicular for both incident laser and emitted PL light with respect to the NW axis.

The band profile in $In_{0.3}Ga_{0.7}N$-GaN NWs was calculated by solving the 3-dimensional nonlinear Poisson equation, discretized with a standard finite-element scheme, for different values of bulk n-type doping. No compositional fluctuations have been considered. Electron and hole densities were calculated based on the standard bulk expressions, using strain-corrected 8-band bulk k·p to calculate band edge energies[46]. The strain was calculated using linear elasticity with natural (zero force) boundary conditions[47]. For the spontaneous and piezoelectric polarization, the nonlinear model described by Prodhomme et al. was applied.[48]. In the Poisson equation, surface states with a density of 6×10^{14} cm^{-2} were used as boundary conditions with energy levels according to Segev et al.[40], and assuming zero electric fields outside the NW. For the calculation of the spectra in Figure 7, we have taken into account that the emission from a dipole oriented orthogonally to the nanowire is partly suppressed.[2] Assuming the case of a small nanowire and an optical relative permittivity of $\varepsilon_r \approx 6.2$, we reduced the orthogonal polarization by a factor of $4/(1+\varepsilon_r)^2 \approx 0.077$.

Conflicts of interest

There are no conflicts to declare.

Acknowledgements

The authors thank the Ministerium für Innovation, Wissenschaft und Forschung des Landes Nordrhein-Westfalen, the Senatsverwaltung für Wirtschaft, Technologie und Forschung des Landes Berlin, and the German Bundesministerium für Bildung und Forschung for funding. Part of the work was funded by the European Regional Development Fund (ERDF) in the project 1.8/07. Authors from Universität Bremen acknowledge financial support of the DFG via projects EI 518-12/1 and RO 2057/16-1. M.R. gratefully acknowledges the support by SALSA, a graduate school of Excellence Initiative of the Deutsche Forschungsgemeinschaft (DFG) and the financial support of the DFG within the Collaborative Research Center 787 (SFB 787).

Notes and references

1 Q. Li, K. R. Westlake, M. H. Crawford, S. R. Lee, D. D. Koleske, J. J. Figiel, K. C. Cross, S. Fathololoumi, Z. Mi and G. T. Wang, *Optics Express*, 2011, **19**, 25528.
2 H. E. Ruda and A. Shik, *Journal of Applied Physics*, 2006, **100**, 024314.
3 *Novel Compound Semiconductor Nanowires*, ed. F. Ishikawa and I. A. Buyanova, Pan Stanford Publishing Pte Ltd, 2017.
4 M. Tchernycheva, A. Messanvi, A. de Luna Bugallo, G. Jacopin, P. Lavenus, L. Rigutti, H. Zhang, Y. Halioua, F. H. Julien, J. Eymery and C. Durand, *Nano Letters*, 2014, **14**, 3515–3520.
5 T. Zhi, T. Tao, B. Liu, Z. Zhuang, . Dai, Y. Li, G. Zhang, Z. Xie, P. Chen and R. Zhang, *IEEE Photonics Technology Letters*, 2016, **28**, 721–724.
6 S. W. Eaton, A. Fu, A. B. Wong, C.-Z. Ning and P. Yang, *Nature Reviews Materials*, 2016, **1**, 16028.

View Article Online
DOI: 10.1039/D2NR05529E

7 R. Yan, D. Gargas and P. Yang, *Nature Photonics*, 2009, **3**, 569–576.
8 J. Wallys, J. Teubert, F. Furtmayr, D. M. Hofmann and M. Eickhoff, *Nano Letters*, 2012, **12**, 6180–6186.
9 S. Hölzel, M. V. Zyuzin, J. Wallys, E. Pouokam, J. Müßener, P. Hille, M. Diener, W. J. Parak and M. Eickhoff, *Advanced Functional Materials*, 2018, **28**, 1802503.
10 K. Maier, A. Helwig, G. Müller, P. Hille, J. Teubert and M. Eickhoff, *Nano Letters*, 2017, **17**, 615–621.
11 T. Kuykendall, P. Ulrich, S. Aloni and P. Yang, *Nature Materials*, 2007, **6**, 951–956.
12 S. Deshpande, J. Heo, A. Das and P. Bhattacharya, *Nature Communications*, 2013, **4**, 1675.
13 L. Rigutti, M. Tchernycheva, A. D. L. Bugallo, G. Jacopin, F. H. Julien, F. Furtmayr, M. Stutzmann, M. Eickhoff, R. Songmuang and F. Fortuna, *Physical Review B*, 2010, **81**, 045411.
14 J. B. Schlager, N. A. Sanford, K. A. Bertness, J. M. Barker, A. Roshko and P. T. Blanchard, *Applied Physics Letters*, 2006, **88**, 213106.
15 H.-Y. Chen, Y.-C. Yang, H.-W. Lin, S.-C. Chang and S. Gwo, *Optics Express*, 2008, **16**, 13465.
16 Corfdir, Pierre and Feix, Felix and Zettler, Johannes K. and Fernández-Garrido, Sergio and Brandt, Oliver, *New Journal of Physics*, 2015, **17**, 033040.
17 *Indium Nitride and Related Alloys*, ed. T. Veal, C. McConville and W. Schaff, CRC Press, 2009.
18 J. C. Li, T. C. Lu, H. M. Huang, W. W. Chan, H. C. Kuo and S. C. Wang, *Journal of Applied Physics*, 2010, **108**, 063508.
19 C. Kölper, M. Sabathil, F. Römer, M. Mandl, M. Strassburg and B. Witzigmann, *physica status solidi (a)*, 2012, **209**, 2304–2312.
20 H.-M. Huang, T.-C. Lu, C.-Y. Chang, S.-C. Ling, W.-W. Chan, H.-C. Kuo and S.-C. Wang, *Journal of Lightwave Technology*, 2011, **29**, 2761–2765.
21 M. Athanasiou, R. M. Smith, Y. Hou, Y. Zhang, Y. Gong and T. Wang, *Applied Physics Letters*, 2015, **107**, 141110.
22 H. K. Park, S. W. Yoon, Y. J. Eo, W. W. Chung, G. Y. Yoo, J. H. Oh, K. N. Lee, W. Kim and Y. R. Do, *Scientific Reports*, 2016, **6**, 28312.
23 Y. Park, C. C. S. Chan, L. Nuttall, T. J. Puchtler, R. A. Taylor, N. Kim, Y. Jo and H. Im, *Scientific Reports*, 2018, **8**, 8124.
24 Y.-J. Lu, H.-W. Lin, H.-Y. Chen, Y.-C. Yang and S. Gwo, *Applied Physics Letters*, 2011, **98**, 233101.
25 E. Chernysheva, Ž. Gačević, N. García-Lepetit, H. P. van der Meulen, M. Müller, F. Bertram, P. Veit, A. Torres-Pardo, J. M. G. Calbet, J. Christen, E. Calleja, J. M. Calleja and S. Lazić, *EPL (Europhysics Letters)*, 2015, **111**, 24001.
26 K. H. Li, Q. Wang, H. P. T. Nguyen, S. Zhao and Z. Mi, *physica status solidi (a)*, 2015, **212**, 941–946.
27 E. Sakalauskas, O. Tuna, A. Kraus, H. Bremers, U. Rossow, C. Giesen, M. Heuken, A. Hangleiter, G. Gobsch and R. Goldhahn, *physica status solidi (b)*, 2012, **249**, 485–488.
28 H. Harima, *Journal of Physics: Condensed Matter*, 2002, **14**, R967–R993.
29 H. Richter, Z. P. Wang and L. Ley, *Solid State Communications*, 1981, **39**, 625–629.
30 R. J. Nemanich, S. A. Solin and R. M. Martin, *Physical Review B*, 1981, **23**, 6348–6356.
31 H.-L. Liu, C.-C. Chen, C.-T. Chia, C.-C. Yeh, C.-H. Chen, M.-Y. Yu, S. Keller and S. P. DenBaars, *Chemical Physics Letters*, 2001, **345**, 245–251.
32 C. Kranert, R. Schmidt-Grund and M. Grundmann, *New Journal of Physics*, 2013, **15**, 113048.
33 H. Siegle, G. Kaczmarczyk, L. Filippidis, A. P. Litvinchuk, A. Hoffmann and C. Thomsen, *Physical Review B*, 1997, **55**, 7000–7004.
34 S. Hernández, R. Cuscó, D. Pastor, L. Artús, K. P. O'Donnell, R. W. Martin, I. M. Watson, Y. Nanishi and E. Calleja, *Journal of Applied Physics*, 2005, **98**, 013511.
35 R. Mata, A. Cros, K. Hestroffer and B. Daudin, *Physical Review B*, 2012, **85**, 035322.
36 A. G. Kontos, Y. S. Raptis, N. T. Pelekanos, A. Georgakilas, E. Bellet-Amalric and D. Jalabert, *Physical Review B*, 2005, **72**, 155336.
37 S.-E. Wu, S. Dhara, T.-H. Hsueh, Y.-F. Lai, C.-Y. Wang and C.-P. Liu, *Journal of Raman Spectroscopy*, 2009, **40**, 2044–2049.
38 K. D. Goodman, V. V. Protasenko, J. Verma, T. H. Kosel, H. G. Xing and D. Jena, *Journal of Applied Physics*, 2011, **109**, 084336.
39 T. Kehagias, G. P. Dimitrakopulos, P. Becker, J. Kioseoglou, F. Furtmayr, T. Koukoula, I. Häusler, A. Chernikov, S. Chatterjee, T. Karakostas, H.-M. Solowan, U. T. Schwarz, M. Eickhoff and P. Komninou, *Nanotechnology*, 2013, **24**, 435702.
40 D. Segev and C. G. Van de Walle, *Europhysics Letters (EPL)*, 2006, **76**, 305–311.
41 J. Lähnemann, P. Corfdir, F. Feix, J. Kamimura, T. Flissikowski, H. T. Grahn, L. Geelhaar and O. Brandt, *Nano Letters*, 2016, **16**, 917–925.
42 R. Calarco, M. Marso, T. Richter, A. I. Aykanat, R. Meijers, A. v.d. Hart, T. Stoica and H. Lüth, *Nano Letters*, 2005, **5**, 981–984.
43 P. Hille, F. Walther, P. Klement, J. Müßener, J. Schörmann, J. Kaupe, S. Mitić, N. W. Rosemann, S. Chatterjee, A. Beyer, K. I. Gries, K. Volz and M. Eickhoff, *Journal of Applied Physics*, 2018, **124**, 165703.
44 P. Neuderth, P. Hille, J. Schörmann, A. Frank, C. Reitz, S. Martí-Sánchez, M. de la Mata, M. Coll, J. Arbiol, R. Marschall and M. Eickhoff, *Journal of Materials Chemistry A*, 2018, **6**, 565–573.
45 M. de la Mata, C. Magen, J. Gazquez, M. I. B. Utama, M. Heiss, S. Lopatin, F. Furtmayr, C. J. Fernández-Rojas, B. Peng, J. R. Morante, R. Rurali, M. Eickhoff, A. F. i Morral, Q. Xiong and J. Arbiol, *Nano Letters*, 2012, **12**, 2579–2586.
46 S. L. Chuang and C. Chang, *Physical Review B*, 1996, **54**, 2491.
47 M. Povolotskyi and A. Di Carlo, *J. Appl. Phys.*, 2006, **100**, 063514.
48 P.-Y. Prodhomme, A. Beya-Wakata and G. Bester, *Phys. Rev. B*, 2013, **88**, 121304.